J. Fluid Mech. (1980), *vol.* 100, *part* 1, *pp.* 41–64
Printed in Great Britain

Laboratory studies of the entrainment zone of a convectively mixed layer

By J. W. DEARDORFF, G. E. WILLIS AND B. H. STOCKTON

Department of Atmospheric Sciences,
Oregon State University, Corvallis, Oregon 97331

(Received 5 September 1979 and in revised form 7 January 1980)

In laboratory experiments of simulated atmospheric mixed layers the entrainment zone is investigated from measurements of horizontally averaged temperature and buoyancy flux, and from visual observations of penetrating thermals using a spread laser beam. The region of negative buoyancy flux of entrainment is found to be confined between the outermost height reached by the few most vigorous penetrating parcels, and by the lesser height where mixed-layer fluid occupies, usually, some 90 to 95 % of the total area. The height of most negative buoyancy flux of entrainment is found to agree roughly with the level at which mixed-layer fluid occupies half the area.

The thickness of the entrainment zone, relative to the depth of the well-mixed layer just beneath, is found to be quite substantial (0·2 to 0·4), and apparently decreases only asymptotically with increasing 'overall' Richardson number, Ri^*. The thickness is not well predicted by parcel theory.

Extensive detrainment is found to occur within the entrainment zone, and adds to the difficulty in defining the position of the local interface between mixed-layer fluid and unmodified fluid.

For typical Ri^* values occurring in the atmosphere, the dimensionless entrainment rate is found to be given satisfactorily by $0{\cdot}25(Ri^*)^{-1}$, although an $(Ri^*)^{-\frac{3}{2}}$ dependence cannot be ruled out by the present data. Entrainment into a neutral layer in the absence of a capping inversion is found to proceed at the expected rate.

1. Introduction

The outermost portion of a mixed layer where non-turbulent fluid is entraining but is not yet incorporated into the well-mixed layer may be called the 'entrainment zone'. The same layer has also been termed the 'transition layer' by Malkus (1958) and Price (1979), the 'more stable layer' by Betts (1973), the 'capping stable layer' by Carson & Smith (1974), and the 'thermocline' or 'thermocline erosion zone' by numerous oceanographers. It is defined in an ensemble-mean or horizontal-average sense, in contrast with the local position of the surface which (when definable) separates mixed-layer fluid from less-turbulent unmodified fluid. The latter surface has been called the 'entrainment interface' by Phillips (1972). The overall zone containing the main convolutions of the entrainment interface constitutes the entrainment zone which is the topic of this paper. The thickness of this zone, to be designated by Δh, is, when horizontally averaged, typically 25 % of that of the well-mixed layer itself. It therefore

0022–1120/80/4517–1800 $02.00

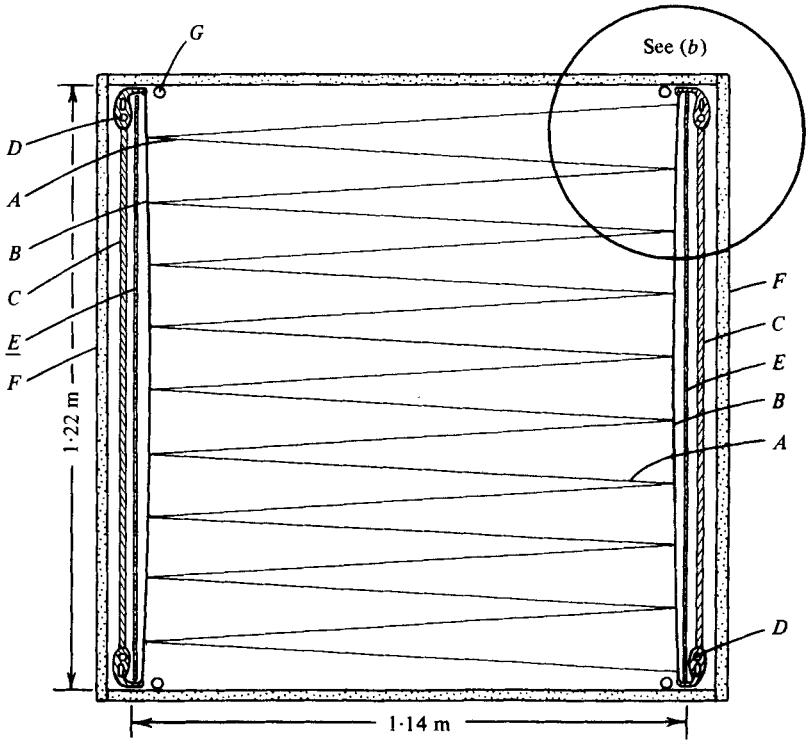

(a)

FIGURE 1 (a). For legend see page 43.

may need to be treated explicitly in mixed-layer growth theories, most of which presently assume its thickness may be neglected. In recent theories of stratocumulus layer growth or maintenance, the positioning of long-wave radiative flux divergence near cloud top has assumed importance (Kahn & Businger 1979; Lilly & Schubert 1980; Randall 1980; Deardorff 1976), and knowledge of how the mixed-layer fluid or cloudy air is distributed within Δh would be very useful.

There is thus considerable incentive to explore the entrainment zone, since existing knowledge of its thickness and structure at the edge of a convectively mixed layer is very scanty. Recently, the laboratory penetrative-convection tank described by Willis & Deardorff (1974) has been modified and utilized for this purpose, and we shall report the results of such studies here.

2. Simulation tank and associated equipment

The laboratory convection chamber used in this study has been described by Willis & Deardorff (1974) and is pictured in figure 1. It has a nearly square horizontal cross-section, 1·14 m by 1·22 m. In preparation for an experiment the tank is first partially filled with a layer of neutrally stratified water at a temperature near 20 °C to a depth of 0·2 m. Above this layer either a stably stratified layer or a less dense neutral layer is laid down with a thickness of about 0·3 m. The water is both degassed and de-ionized. An experiment commences when hot water is circulated underneath and in contact with the bottom aluminium plate of the tank. The bottom plate temperature

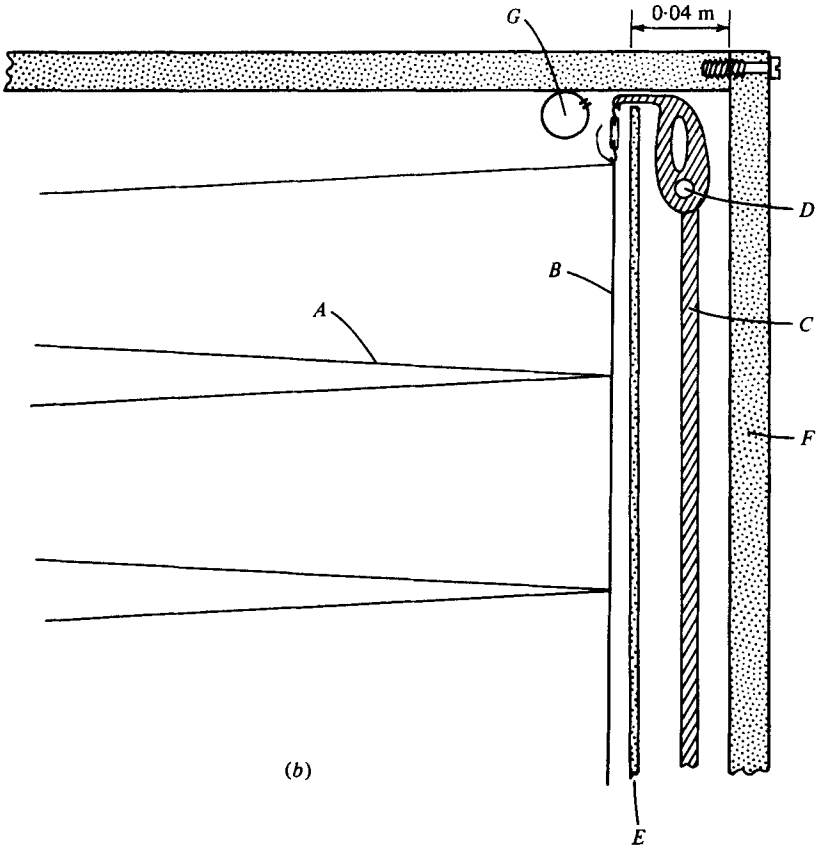

FIGURE 1. (*a*) View from above of the convection chamber, showing T-bar wire, A; its two insulated support wires of 0·6 mm diameter, B; two support rods, C, and four vertical support rods, D; the two vertical plastic side partitions which isolated the T-bar support rods, E; the tank acrylic plastic side walls, F; and the four siphon pipes in the corners, G, which provided horizontal divergence. (*b*) An enlargement of the circled portion of (*a*), showing one of the four corner supports for the T-bar wire.

thus produced is nearly uniform in the horizontal (the root-mean-square temperature variations being about 1·6 % of the mean surface to mixed-layer temperature drop). After thermal convection is initiated the lower neutral layer quickly becomes a turbulent mixed layer and then advances gradually into the outer stable layer or less dense layer. Various initial conditions have been utilized, leading usually to a mixed-layer growth from 0·03 m to 0·15 m over a time period of 10 to 20 min.

In most of the experiments a constant horizontal velocity divergence is applied by means of vertical siphoning pipes (with evenly spaced holes along the vertical) located one in each of the four corners of the tank. This gradual mass sink yields a mean subsidence rate which, at the top of the mixed layer, has a magnitude of from 10 % to 100 % of the entrainment rate. The motivation for this system was to suppress weak secondary circulations apparently arising from the corners of the tank, but it also serves to simulate large-scale oceanic upwelling or atmospheric subsidence.

Horizontally averaged temperature within the convecting water is measured

through use of a long, fine (0·08 mm) resistance-wire thermometer (T bar wire) shown in figure 1(*a*). Its main supporting members are located behind vertical partitions just inboard of the outer tank side walls, as shown in figure 1(*b*), in order to avoid excessive wake effects when the system is moved vertically. The wire encompasses a horizontal plane of the tank by extending back and forth horizontally across the tank 20 times. Its mean height is adjustable and determined to a relative accuracy of 0·1 mm and an absolute accuracy of 1 mm. One or two thermocouples are located at the same height as the T-bar wire for purposes of exploring the local interface as well as for calibrating the T-bar wire just before convection is initiated in each experiment. The T-bar wire and thermocouples are programmed to cycle repeatedly during an experiment from a height of about 0·4 m down to 0·02 m and back, at a speed usually set at 0·01 m s^{-1}. The mean temperature has a relative accuracy of about 0·01 °C.

From various tests it has been determined that the signal produced by the T-bar wire was proportional only to mean temperature and not to the vertical traversing speed or to strain gauge effects. Effects of the wire and thermocouple wakes are believed to be small in comparison with those of spurious secondary circulations possibly induced by the walls or persisting after filling the tank. The latter effect gave rise to spurious 'turbulent' heat fluxes with magnitude of about 2 % of the surface input heat flux.

A 5 mW He–Ne laser beam of thickness 1 mm can be passed through one of the acrylic side walls of the tank to determine the spatial distribution of mixed-layer fluid when the latter contains a dilute solution of milk. This laser is used in one of three different modes of illumination: (1) for visually estimating at various heights the percentage area occupied by mixed-layer fluid, the beam is spread horizontally with a cylindrical (rod-shaped) lens to cover the entire tank area; (2) for photographing horizontal planforms, the entire tank area is illuminated by rotating the beam horizontally along an arc while the camera shutter is held open for about 10 s; and (3), for photographing a vertical cross-section, the horizontally directed beam is traversed vertically over the depth of the mixed layer while the camera shutter is held open for about 25 s. In the latter two modes of operation, the beam thickness is about 2 mm.

The raw data are digitized at a rate of 200 points per second per variable and written onto magnetic tape for analysis. In the analysis, the temperature and height data are averaged in groups of 16, leaving one data point per variable for each 0·8 mm along a vertical traverse.

In the computer analysis the turbulent heat flux is determined from the vertically integrated, horizontally averaged thermodynamic equation:

$$\overline{w'\theta'}(z) = \int_z^{h_3} (\partial\overline{\theta}/\partial t + \overline{w}\,\partial\overline{\theta}/\partial z)\,dz + \kappa[\partial\overline{\theta}/\partial z - (\partial\overline{\theta}/\partial z)_3],$$

where θ refers to temperature in the convection tank (or to virtual potential temperature in the atmosphere), the subscript 3 refers to a height in excess of the uppermost reaches of the mixed layer where $\overline{w'\theta'}$ can be assumed to be essentially zero, the overbar refers to the horizontal average, and κ is the thermal diffusivity of water, taken to be 0·145 $mm^2\ s^{-1}$.

3. Distribution of mixed-layer fluid within Δh

Photographs of mixed-layer fluid at five relative heights (ζ) within the entrainment zone are shown in figure 2 (*a*)–(*e*) (plate 1). The relative height, ζ, is defined by

$$\zeta = (z - h_0)/\Delta h, \tag{1}$$

where z is height, h_0 is the particular height near the top of the thoroughly mixed layer where the turbulent heat flux first reaches zero, and Δh is defined as

$$\Delta h = h_2 - h_0, \tag{2}$$

where h_2 is the smallest height beyond which the buoyancy flux and its vertical derivative remain vanishingly small. As will be seen later, h_2 corresponds very closely to the outermost height to which only a few penetrating elements barely reach at any given time, and h_0 corresponds to a height where only a small percentage of the fluid remains unmodified and unmixed.

At $\zeta = 0{\cdot}87$, figure 2 (*a*) reveals the presence of several penetrating plumes of small diameter, some of which appear in clusters having a common 'parent' dome just beneath. At this height and time the fractional area (A) covered by mixed-layer matter is estimated to have been 0·012. Figures 2 (*b*)–(*e*) show monotonically increasing mixed-layer cover, A, at decreasing relative heights: $A = 0{\cdot}063$, 0·13, 0·31, and 0·52 at $\zeta = 0{\cdot}77$, 0·71, 0·60, and 0·46, respectively. The photographs were all taken during a single experiment, *E* 7 of table 1, at the fixed height of 0·278 m while h_0 increased and ζ decreased.

For reference, profiles of the mean potential temperature (or virtual potential temperature in the atmospheric analogue) and turbulent heat flux occurring approximately at the times of figures 2 (*a*)–(*e*) are presented in figures 3 and 4, respectively. The temperature profiles indicate that this case was one of nearly constant stratification aloft; the horizontal divergence, of magnitude $8{\cdot}8 \times 10^{-5}$ s^{-1}, produced subsidence at $z = h_0$ which retarded the mixed-layer growth rate by some 38 %. Profiles (*a*) and (*e*) were obtained while the long resistance wire was moved downwards. Consequently, they exhibit a slightly more superadiabatic-appearing mixed layer than that which exists instantaneously, since at any height within the mixed layer $\overline{\theta}$ increases slowly with time as the sensor moves toward the lower boundary. Similarly, profiles (*b*)–(*d*), gathered in the upward direction, appear slightly less adiabatic than the instantaneous mean state.

The profiles of heat flux $\overline{(w'\theta')}$ were each derived from a pair of successive upward or downward profiles of $\overline{\theta}$, and represent an average over a 75 s time interval (corresponding to about 3 convective time scales $\tau = h_0/w_*$, where w_* is the mixed-layer convective velocity scale). Each heat-flux profile is centred in time with the correspondingly labelled temperature profile. By doubling the averaging time over which $\overline{w'\theta'}$ profiles were calculated in a typical experiment, it was determined that the estimate of Δh was increased by only 7 %. This verifies the photographic evidence that the considerable magnitude of Δh, relative to h_0, is a real feature and not an artifice of the data collection or analysis methods.

At the height of most negative buoyancy flux, the ratio of the molecular heat flux to the total heat flux lies in the 5–15 % range in our experiments. This ratio approaches

Desig-nation	Time (s) §	$\Delta h/h_0$	Ri^*	$\bar{h}$ (m)	Δh (m)	θ_0 (°C)	$\Delta\theta$ (°C)	$g\beta(\theta_0)$ (mm s^{-2} °C^{-1})	w_* (mm s^{-1})	$-\overline{w}(\bar{h})$ (mm s^{-1})	$\Gamma(h_2)$ (°C m^{-1})	$\frac{(d\bar{h}/dt - \overline{w}_h)}{w_*}$	$\frac{(dh_0/dt - w_0)}{w_*}$	$\frac{(d\Delta h/dt - \Delta w)}{w_*}$
*E*1	313	0·259	19·4	0·226	0·053	18·23	3·43	1·98	8·89	0·020	95	0·0137	0·0116	0·0038
	464	0·244	23·4	0·240	0·053	19·30	3·70	2·07	8·86	0·021	103	0·0109	0·0117	−0·0015
	615	0·224	26·1	0·249	0·051	20·25	3·83	2·15	8·86	0·022	102	0·0091	0·0092	−0·0016
	765	0·209	27·8	0·257	0·049	21·07	3·78	2·22	8·81	0·023	115	0·0079	0·0076	−0·0011
*E*2	277	0·349	15·3	0·243	0·076	22·50	2·32	2·34	9·30	0·022	10†	0·0178	0·0143	0·0094
	389	0·372	12·3	0·260	0·086	23·19	1·81	2·38	9·56	0·023	1·7	0·0189	0·0171	0·0132
	502	0·399	8·5	0·280	0·099	23·87	1·11	2·43	9·45	0·025	1·7	0·0243	0·0206	0·0110
	577	0·405	7·0	0·295	0·106	24·22	0·88	2·47	9·54	0·027	1·7	0·0251	0·0267	0·0114
*E*3	350	0·321	25·4	0·220	0·063	20·63	4·19	2·18	8·88	0·019	85	0·0140	0·0146	0·0020
	630	0·300	36·2	0·242	0·065	22·50	4·97	2·33	8·78	0·020	85	0·0099	0·0091	0·0025
	956	0·276	45·1	0·257	0·064	24·16	5·28	2·46	8·58	0·021	97	0·0069	0·0068	0·0001
*E*4	351	0·280	24·0	0·230	0·058	22·77	3·75	2·36	9·21	0·022	93	0·0129	0·0118	−0·0004
	651	0·236	31·6	0·253	0·054	24·55	4·31	2·40	9·07	0·024	92	0·0092	0·0087	0·0000
	989	0·192	36·2	0·267	0·047	26·24	3·98	2·64	8·76	0·025	105	0·0059	0·0026	0·0014
*E*5	256	0·339	16·5	0·255	0·076	20·81	2·64	2·20	9·46	0·000	8·3†	0·0144	0·0142	0·0080
	367	0·357	13·7	0·271	0·085	21·51	2·05	2·26	9·57	0·000	3·3	0·0142	0·0131	0·0109
	514	0·399	9·5	0·293	0·103	22·31	1·31	2·32	9·69	0·000	1·0	0·0188	0·0161	0·0142
	624	0·406	5·9	0·320	0·114	22·90	0·73	2·37	9·66	0·000	1·0	0·0325	0·0311	0·0067
*E*6	409	0·364	13·6	0·266	0·086	21·42	2·14	2·25	9·71	0·024	33	0·0281	0·0248	0·0028
	559	0·318	18·3	0·299	0·085	22·30	2·43	2·32	9·61	0·027	35	0·0215	0·0245	−0·0027
	747	0·275	19·0	0·328	0·082	23·15	2·43	2·38	10·00	0·030	12	0·0162	0·0182	−0·0015
*E*7	388	0·260	21·9	0·241	0·057	19·11	3·65	2·06	9·10	0·021	93	0·0124	0·0143	−0·0007
	610	0·223	27·1	0·258	0·053	20·53	3·95	2·18	9·05	0·023	97	0·0091	0·0126	−0·0037
	980	0·172	29·4	0·275	0·044	22·42	3·70	2·33	8·98	0·024	107	0·0057	0·0076	−0·0029
*E*8	216	0·382	9·8	0·263	0·092	21·46	1·53	2·25	9·61	0·023	17	0·0476	0·0373	0·0112
	328	0·387	11·3	0·304	0·104	22·06	1·57	2·30	9·86	0·027	15	0·0360	0·0367	0·0243
*E*9	352	0·286	19·3	0·240	0·062	19·38	3·25	2·08	9·18	0·022	63	0·0160	0·0164	−0·0034
	577	0·256	24·0	0·263	0·061	20·74	3·46	2·20	9·14	0·024	62	0·0129	0·0122	0·0006
	877	0·236	28·3	0·285	0·061	22·25	3·58	2·32	9·15	0·026	53	0·0080	0·0104	−0·0005

$E10$	328	0·262	16·5	0·227	0·054	21·19	3·26	2·23	9·14	0·020	77	0·0147	0·0138	0·0009
	553	0·224	21·4	0·246	0·051	22·63	3·70	2·35	9·25	0·021	90	0·0097	0·0110	−0·0006
	816	0·198	24·8	0·262	0·048	24·13	3·83	2·47	9·11	0·023	103	0·0083	0·0082	−0·0014
$E11$	252	0·359	13·8	0·246	0·078	22·90	2·21	2·37	9·67	0·023	3·3	0·0158	0·0141	0·0053
	402	0·374	9·6	0·269	0·089	23·87	1·31	2·44	9·44	0·025	3·3	0·0228	0·0210	0·0088
$E12$	360	0·251	76·0	0·217	0·050	19·75	13·33	2·11	8·96	0·020	315†	0·0057	0·0098	−0·0083
	549	0·210	82·9	0·220	0·043	21·32	12·76	2·24	8·71	0·020	280†	0·0023	0·0034	−0·0026
	774	0·201	82·0	0·218	0·041	22·84	11·49	2·36	8·49	0·020	270†	0·0014	−0·0002	0·0019
	961	0·234	79·2	0·216	0·046	23·56	10·21	2·42	8·21	0·020	262†	0·0015	−0·0028	0·0046
$E13$	364	0·360	58·3	0·190	0·062	20·67	10·60	2·19	8·70	0·030	417†	0·0144	0·0145	0·0026
	600	0·269	80·0	0·201	0·050	22·62	12·41	2·35	8·56	0·032	295†	0·0057	0·0074	−0·0085
	777	0·242	82·4	0·202	0·045	23·87	11·64	2·45	8·36	0·032	300†	0·0033	0·0002	−0·0026
	954	0·236	84·6	0·200	0·043	24·86	10·90	2·52	8·06	0·031	273†	0·0022	0·0013	−0·0049
$E14$	330	0·256	17·0	0·232	0·054	20·47	2·94	2·18	9·34	0·022	57	0·0158	0·0146	0·0015
	472	0·244	20·2	0·247	0·055	21·42	3·12	2·25	9·26	0·023	43	0·0124	0·0131	0·0008
	695	0·234	24·5	0·266	0·057	22·69	3·36	2·35	9·26	0·025	55	0·0109	0·0095	0·0008
	995	0·220	28·0	0·282	0·057	23·99	3·17	2·45	8·84	0·027	50	0·0087	0·0087	0·0006
$E15$	355	0·226	31·7	0·238	0·049	19·74	5·42	2·12	9·29	0·022	75†	0·0073	0·0072	0·0009
	688	0·231	28·5	0·252	0·053	21·86	3·96	2·29	8·96	0·023	28†	0·0067	0·0057	0·0023
	1021	0·240	21·9	0·264	0·058	23·55	2·68	2·42	8·84	0·024	8·3†	0·0076	0·0066	0·0045
	1355	0·304	16·2	0·282	0·078	24·78	1·59	2·52	8·35	0·026	1·7	0·0111	0·0082	0·0142
$E16$‡	89	0·619	9·6	0·075	0·039	23·77	2·05	2·44	6·26	0·000	70†	0·0197	0·0342	−0·0179
	153	0·527	5·5	0·086	0·039	24·83	1·06	2·52	6·44	0·000	3·3	0·0349	0·0425	0·0046
	217	0·484	1·9	0·108	0·046	25·65	0·32	2·58	6·86	0·000	1·3	0·0525	0·0493	0·0511

† Close above $z = h_2$, Γ decreased to a much smaller value of order 1 °C m^{-1}, and the fluid configuration appeared like a two-layer system.
‡ For the $E16$ experiment the depth of the initial neutral layer was 0·07 m instead of 0·20 m.
§ Times refer to elapsed time after initiation of convection.

TABLE 1. Supplementary data.

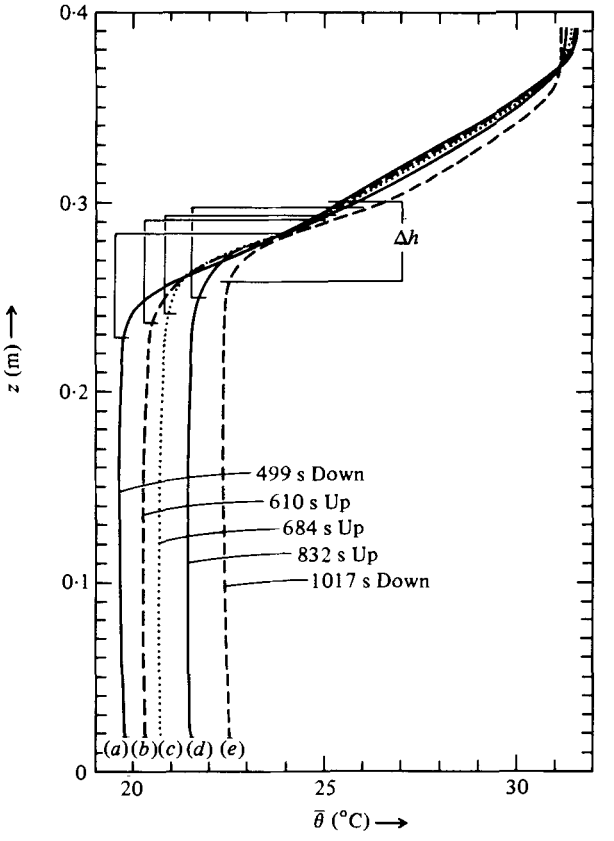

FIGURE 3. Horizontal-mean temperature profiles in $E7$ occurring at about the same times as photos (*a*)–(*e*) of Fig. 2. The labels Down and Up refer to direction of movement of the resistance-wire thermometer during the traversing measurement. Brackets on upper parts of profiles denote the entrainment zone, Δh, based upon time-smoothed analyses of h_2 and h_0.

100 % as $z \to h_2$. The latter fact implies that mixed-layer turbulence rarely reaches h_2, and does not imply that what turbulence does occur there is weak.

Within the layer Δh, variable amounts of mixed-layer fluid are seen to coexist with unmodified fluid in figure 2. Using the horizontally spread laser beam, the fraction A of mixed-layer fluid existing at a given height ζ was determined visually from two particular experiments of different types: $E1$, constant positive stratification aloft ($\Gamma\Delta h/\Delta\theta = 1{\cdot}25$, where $\Delta\theta$ is the strength of the capping inversion across Δh, and Γ is the rate of change of mean potential temperature with height at $z = h_2$); and $E2$, a nearly two-layer system with Γ quite small ($\Gamma\Delta h/\Delta\theta = 0{\cdot}04$). Subsidiary data on $E1$ and $E2$ are supplied in table 1. The results of the two experiments are shown in figures 5 and 6, respectively, where $1-A$ is presented as the lower abscissa. Within the accuracy of the estimations of A by eye (probably $\pm$ 10 % for either A or $1-A$, whichever is the smaller) both experiments $E1$ and $E2$ exhibit the same general distribution. (Error bars in the vertical direction are associated with small uncertainties in h_0 and Δh.)

Both figures 5 and 6 indicate that at $z = h_0$ the fraction of mixed-layer fluid is some 90 to 95 %. Only at considerably smaller heights can the fluid be considered to be

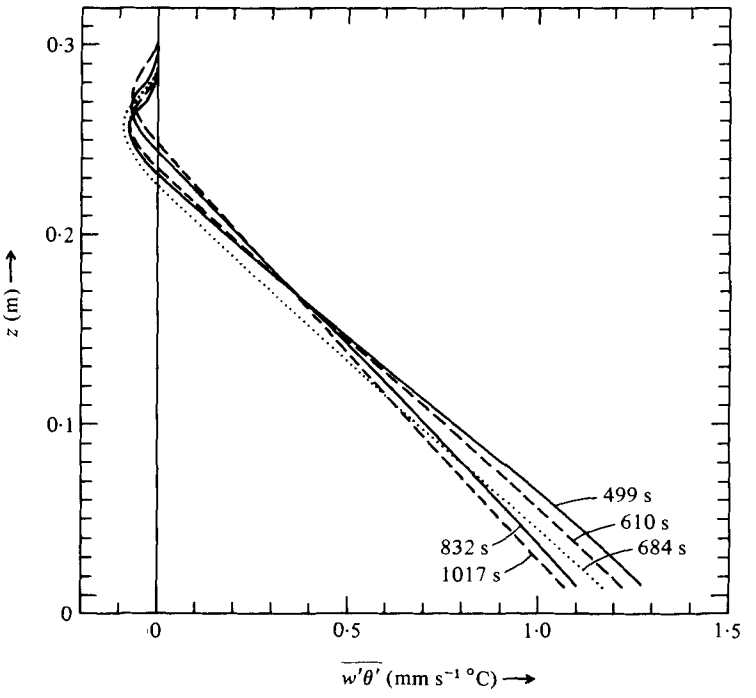

FIGURE 4. Mean profiles of kinematic turbulent heat flux at the respective times of the $\bar{\theta}$ profiles of figure 3. The molecular heat flux is not included within the abscissa variable.

99 % mixed, for example, and then only if the entrainment rate, relative to the convective velocity scale, w_*, is not too great (not exceeding about 0·03 to 0·04).

In the central portion of the entrainment zone $A(\zeta)$ is seen to decrease very rapidly, and nearly linearly, with height. A long tail of small A values extends up towards $z = h_2$. The existence of such a tail is not too surprising, since the updrafts existing at $z = h_0$ must possess a statistical distribution such that only a tiny fraction have velocities greatly in excess of the standard deviation at h_0. Thus, only a tiny fraction of mixed-layer material will have penetrated to $z = h_2(t)$ at any given time. These highest domes are very transitory, falling back rapidly, after over-shooting, into broader domes just underneath.

The one-to-one correspondence between $A(\zeta)$ and certain features of $\overline{w'\theta'}(\zeta)$ is shown in figure 7 for experiment E 1 and in figure 8 for E 2. These and other like results form the basis for our conclusion that h_2 occurs at the greatest height to which very small amounts of mixed-layer fluid can penetrate. In addition, the height of most negative buoyancy flux, $\bar{h}$, is usually found to occur where A is about 0·5 as in these examples. For purposes of estimating representative values of h_2 and h_0, we have used smooth curves faired through the h_2 and h_0 data points, as in figures 7 and 8.

For reference, in figure 5 the scaled temperatures

$$\hat{\theta} = (\bar{\theta} - \theta_0)/(\theta_2 - \theta_0), \tag{3a}$$

$$\hat{\theta}_m = (\bar{\theta} - \theta_m)/(\theta_2 - \theta_m), \tag{3b}$$

$$\hat{\theta}_{en} = (\bar{\theta} - \theta_m)/[\theta_{en}(z) - \theta_m] \tag{3c}$$

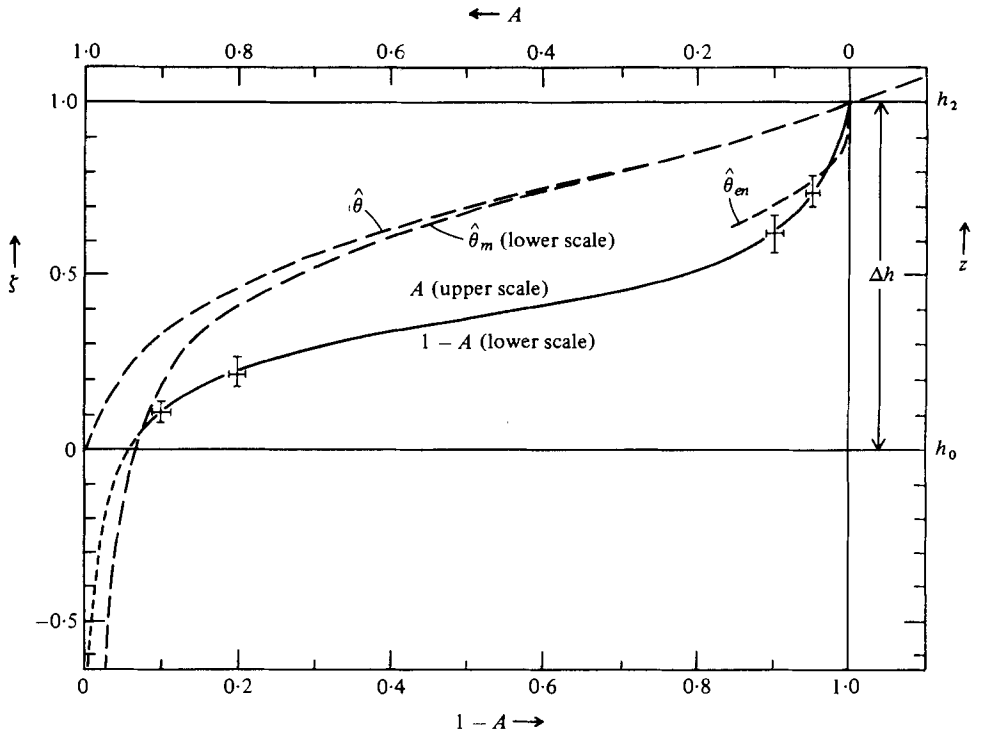

FIGURE 5. Fraction of mixed-layer fluid, A (upper abscissa), as a function of relative height, ζ, within the entrainment zone for experiment $E1$. Profiles of normalized mean potential temperature $\hat{\theta}$, $\hat{\theta}_m$ and $\hat{\theta}_{en}$ (see (4)) shown refer to the lower abscissas, on which $1-A$ is also plotted.

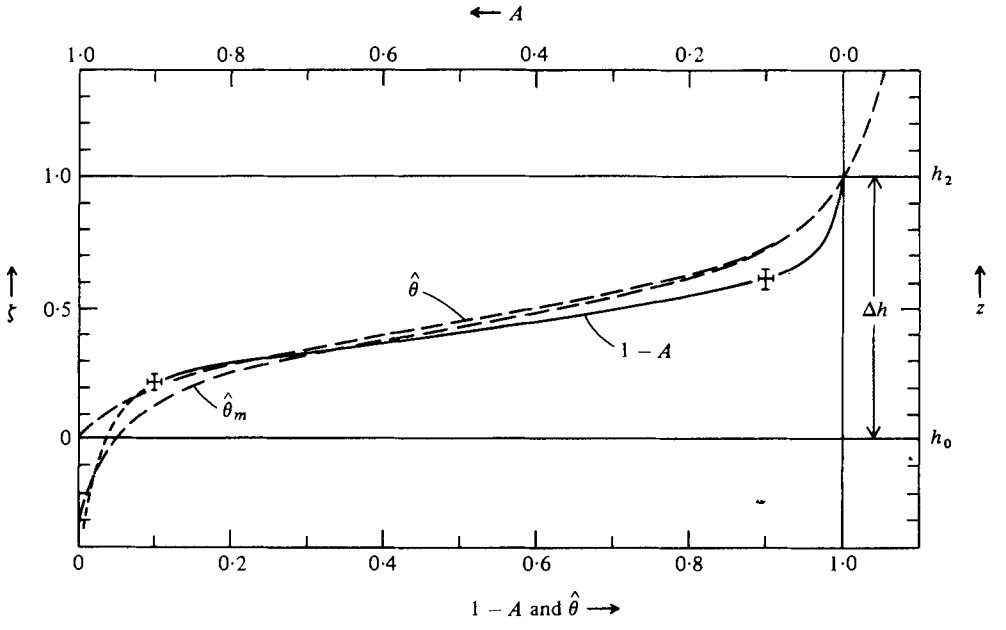

FIGURE 6. Fraction of mixed-layer fluid, A (upper abscissa), as a function of relative height, ζ, within the entrainment zone for experiment $E2$. Profiles of normalized mean potential temperature, $\hat{\theta}$ and $\hat{\theta}_m$, are also shown.

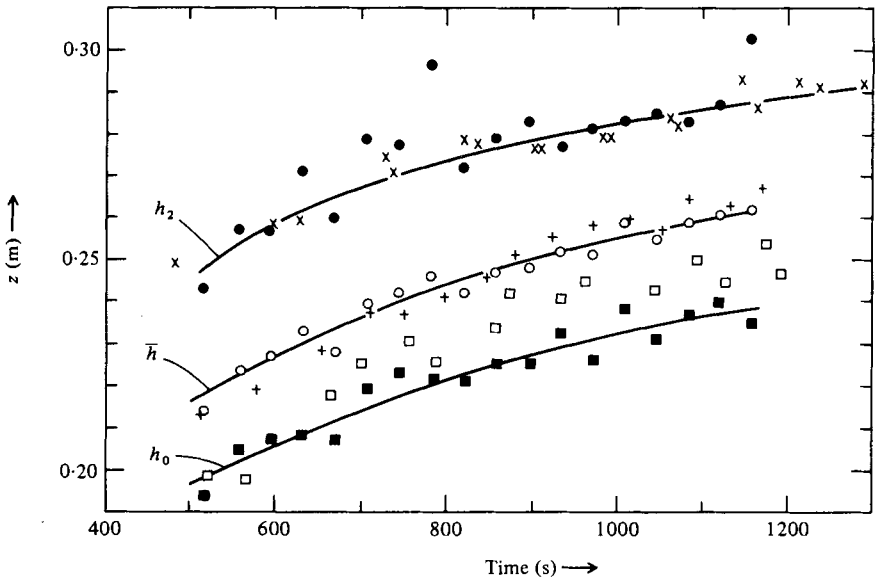

FIGURE 7. Evolution of h_2, $\bar{h}$ and h_0 for experiment $E1$ as determined from many individual buoyancy-flux profiles. Also plotted from visual laser determinations are the height of greatest penetration of a thermal element at the given time (×), the height of 50 % mixed-layer coverage (+) and the estimated height of 90 % mixed-layer coverage (□). ●, h_2 from $\overline{w'\theta'}(z)$; ○, $\bar{h}$ from $\overline{w'\theta'}(z)$; ■, h_0 from $\overline{w'\theta'}(z)$.

are also presented, where θ_2 and θ_0 are $\bar{\theta}$ at $z = h_2$ and h_0, respectively, θ_m is the mixed-layer potential temperature at $z = \frac{1}{2}h_0$, and $\theta_{en}(z)$ is the unmodified value of $\bar{\theta}(z)$ existing a short time earlier. There is considerable similarity between the quantity $(1-A)$ and the scaled temperature $\hat{\theta}_{en}$ defined by (3*c*), and in figure 6 with $\hat{\theta}_m$ which for the two-layer system amounts to the same quantity as $\hat{\theta}_{en}$. The similarity comes about because $\bar{\theta}(\zeta)$ can be considered to a first approximation to be formed from a bimodal distribution of fluid elements having either the temperature θ_m or the unmodified environmental temperature $\theta_{en}(z)$:

$$\bar{\theta}(z) \approx A\theta_m + (1-A)\,\theta_{en}(z). \tag{4a}$$

Hence,
$$\bar{\theta} - \theta_m \approx (1-A)\,(\theta_{en} - \theta_m)$$

and
$$(\bar{\theta} - \theta_m)/(\theta_{en} - \theta_m) \approx 1 - A = \hat{\theta}_{en}. \tag{4b}$$

In figure 5 the $\hat{\theta}_{en}$ curve does not extend far, however, because of difficulty in estimating $\theta_{en}(z)$ of the stably stratified, entraining fluid existing between mixed-layer hummocks. Other reasons for inexactness of (4*b*) involve modification of mixed-layer fluid within Δh by small-scale entrainment, and modification of 'environmental' fluid by detrained mixed-layer fluid to be discussed in § 4.

4. Detrainment

Close inspection of figures 2(*c*)–(*e*) reveals regions of mixed-layer fluid that appear stringy or tenuous and without sharp boundaries. These areas contrast strongly with the more prevalent, sharply defined regions that contain 100 % mixed-layer fluid

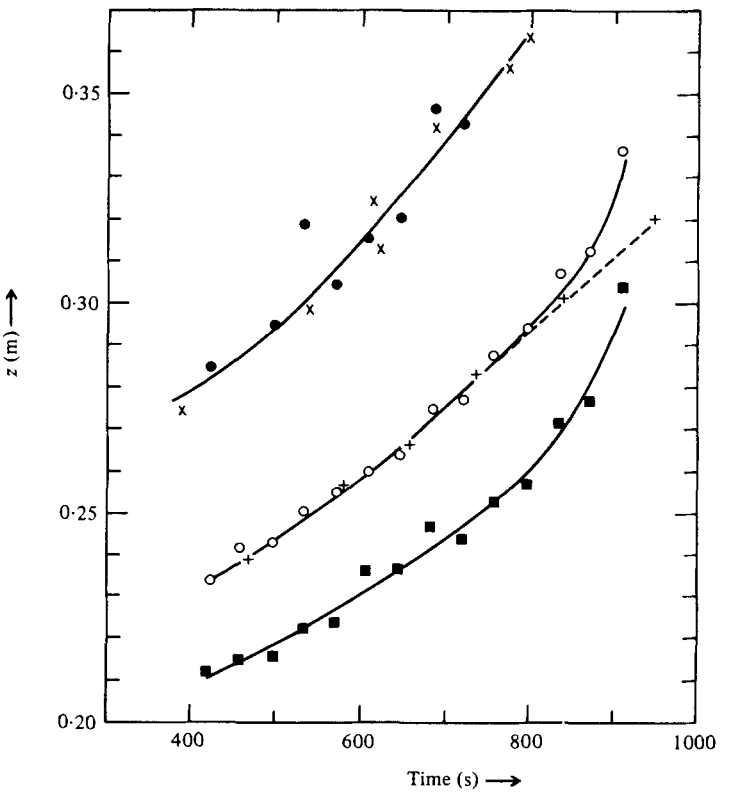

FIGURE 8. Evolution of h_2, $\bar{h}$ and h_0 for experiment $E2$ as determined from many individual buoyancy-flux profiles. Also plotted from visual laser determinations are the height of greatest penetration of a thermal element ($\times$), and the height of 50 % mixed-layer coverage (+). ●, h_2; ○, $\bar{h}$; ■, h_0.

(except for occasional intrusions or entrapment of entraining fluid). Evidently, the stringy regions represent mixed-layer fluid that has become detached from the top of the mixed layer and sheared out – debris ejected from mixed-layer domes when vortices or breaking internal waves occur at their edges. This process is called 'detrainment', since it is the reverse of entrainment. (An extreme example of detrainment is the decay of a tall, penetrating convective cloud or its outflowing anvil; see Namias 1939.)

Side views within the mixed layer support this conclusion. Regions of formation of detrained fluid are identified in the x, z plane views of figures 9 (a), (b). The illuminated vertical slice, being only 2 mm thick ($0{\cdot}008\bar{h}$ thick), permits the small-scale features to be observed much more readily than was possible in the study of Deardorff, Willis & Lilly (1969). These relatively small scales occur even in the laboratory because the Kolmogorov length scale $(\nu^3/\epsilon)^{\frac{1}{4}}$, where ν is the kinematic viscosity and ϵ is the average rate of dissipation within Δh, at the height $\bar{h}$ was only 1·2 mm. The short arrows point to small regions of vortical motion or individual Kelvin–Helmholtz-like billows where mixed-layer matter is in the process of being detrained. The long arrows point to regions where detrained debris persists. Vorticity with a vertical component,

located at the side edges of mixed-layer domes, also appears to be important in producing detrainment, as suggested from figures 2(*c*)–(*e*).

The detrained fluid remains visible for considerable periods of time because of reduced turbulent diffusion after being cut off from the rest of the mixed layer. However, it is gradually swept back into the mixed layer by the entrainment process, which must be aided by residual negative buoyancy which the detrained fluid possesses. Thus, a quasi-steady distribution of detrained fluid exists at any given time within Δh, due to a balance between rate of detrainment and subsequent re-entrainment. At $\zeta = 0{\cdot}5$ up to 30 % of the mixed-layer fluid visible appears to be detrained debris, for typical values of capping-inversion stability. (This estimate is an upper limit because of the tenuity of the detrained fluid.) This fraction diminishes upwards, and in the cases we have examined becomes negligible above $\zeta = 0{\cdot}9$. Below $\zeta \approx 0{\cdot}4$ we are unable to distinguish clearly between the original and detrained mixed-layer fluid.

Similarly detrained mixed-layer fragments are evident in casual observations of fair-weather cumulus clouds, although, because of rapid evaporation of cloud material, they do not stay visible for nearly as long as would a conservative tracer such as smoke. Strong evidence of detrainment near the tops of stratocumulus clouds capping a mixed layer has been presented by Goodman & Miller (1976).

In figures 5 and 6 the estimates of A include the detrained matter, since the latter helps modify the mean state within Δh. However, for some purposes, such as likening $A(z)$ to a turbulence intermittency factor, the detrained matter should not be included within A.

Rayment & Readings (1974) have emphasized the importance of billows at the tops of the larger domes in promoting entrainment. We find that the individual billow or breaking wave, though it promotes strong mixing, appears to induce at least as much detrainment as entrainment. Later, the detrained matter disappears into the larger cusps located in regions of horizontal convergence and entrainment near the base of the entrainment zone. In figure 9(*a*) (plate 2), the primary regions of large-scale entrainment are in the centre, the far left, and possibly near the far right; in figure 9(*b*), 12 min later, regions of large-scale entrainment appear to be near the far left and right only, in this vertical slice.

5. Analogy between mixed-layer hummocks and cumulus clouds

It may have been noticed that the uppermost portions of the mixed layer seen in figure 9 resemble fair-weather cumulus clouds. The resemblance can be enhanced by illuminating the upper mixed layer in depth, when mixed-layer fluid has been dyed white, but illuminating only above a particular height that would correspond to cloud-base height, or lifting condensation level. This procedure was followed to obtain figure 10 (plate 3), where the resemblance to cumulus-humilis clouds is striking. For shallow atmospheric cumulus less than about 50 m in vertical extent, the condensational warming is usually only a small fraction of $\Delta\theta$. Therefore, the clouds then serve merely as markers of the upper reaches of a clear mixed layer.

Identification of shallow cumulus with the more pronounced hummocks at the top of the atmospheric mixed layer has previously been made by Uthe (1972) using lidar, and by Gaynor & Mandics (1978) using acoustic radar.

6. Behaviour of Δh

The simplest assumption for Δh, which has been used by Betts (1976), is of the nature

$$\Delta h = \alpha' h_0, \tag{5}$$

where α' is a constant of order 0·3.

Another prediction which, however, considers the extent of overshoot of an upward-penetrating parcel (e.g., see Phillips 1977), is

$$\Delta h = c' h_0 Ri^{*-1}, \tag{6}$$

where c' is a constant of order unity and Ri^* is an 'overall' Richardson number defined by

$$Ri^* = g\beta \Delta\theta \bar{h}/w_*^2. \tag{7}$$

Here, g is the gravitational acceleration, β is the coefficient of thermal expansion ($1/\bar{\theta}$ in the atmosphere), and w_* is the turbulent velocity scale for a convectively mixed layer, taken to be

$$w_* = [g\beta(\overline{w'\theta'})_s \bar{h}]^{\frac{1}{3}}, \tag{8}$$

where $g\beta(\overline{w'\theta'})_s$ is the kinematic buoyancy flux at the surface, or heat source. Although (6) is more comprehensive than (5), its derivation neglects (*a*) effects of turbulent diffusion upon a parcel of mixed-layer fluid that is rising within Δh, (*b*) the non-hydrostatic pressure perturbation at the top of the rising parcel, (*c*) the effect of mixed-layer fluid already existing elsewhere at the same height as the penetrating parcel in question, and (*d*) any dependence upon Ri^* of the vertical velocity (relative to w_*) which the parcel possessed at $z = h_0$. A derivation of (6) and modifications to it which address considerations (*c*) and (*d*) are presented in the appendix.

In a series of experiments we have ascertained $\Delta h = h_2 - h_0$ through indirect measurement of turbulent heat-flux profiles, as described in § 2, to give h_2 and h_0, and by laser illumination to verify h_2. Conditions and results of these experiments are also listed in table 1. A plot of $\Delta h/h_0$ versus Ri^* is shown in figure 11. Although there is much more data scatter than we can explain, there is little support for either (5) or (6) alone. The scatter is systematic in that the results of any given experiment, from which two to four values of $\Delta h/h_0$ were extracted, were essentially reproducible. It appears that considerations other than Ri^* are important, such as the rate of change of Ri^* or of Γ.

In our experiments intended to treat a two-layer system, Δh usually decreased with time at first as the uppermost penetration height h_2 worked its way up toward the base of the pre-established neutral layer aloft. Then Γ was large. After h_2 reached this height, $\Delta h/h_0$ increased with time as $\Delta\theta$ and Ri^* decreased and Γ was small (data points are then denoted by x).

In figure 11 the dashed curve is

$$\Delta h/h_0 = 0{\cdot}21 + 1{\cdot}31(Ri^*)^{-1}. \tag{9}$$

The suggestion that an asymptotic value for $\Delta h/h_0$ of order 0·2 exists is very surprising, although a theory of Long & Kantha (1978) seems to imply the same. The simplest empirical refinement to the derivation of (6) which will produce (9) is given in the

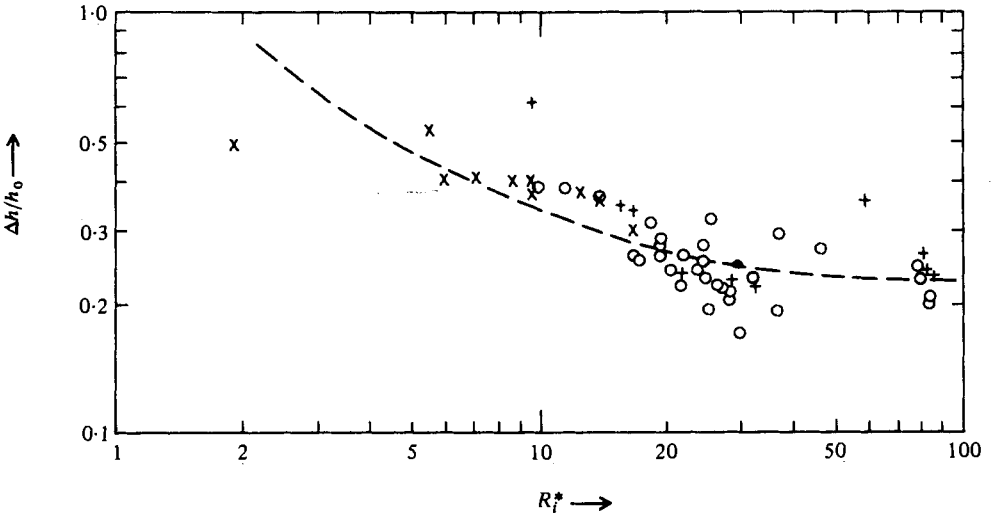

FIGURE 11. Log–log plot of $\Delta h/h_0$ *versus* Ri^* defined in (7). ○, experiments with strong stratification aloft ($\Gamma > 5$ °C cm^{-1}); ×, experiments with a nearly neutral layer aloft to which height h_2 had essentially penetrated; +, data similar to ×'s except that h_2 had not penetrated to the neutral layer aloft.

appendix. There it is concluded that even a modified parcel theory requires stronger vertical velocities at $z = h_0$ than are available, at least for large Ri^*, to explain the relatively large magnitude of Δh. The same result was obtained by Price (1979) who found $\Delta h \approx \frac{1}{3}h_0$ in an ocean mixed layer. However, he concluded that the transition layer is only slightly penetrated by parcels, while we conclude that assumptions of the parcel theory are faulty.

There may be some question if, in our experiments, the Péclet number, Pe, for which one definition is

$$Pe = w_* \bar{h}/\kappa$$

was sufficiently large that $\Delta h/h_0$ would not be affected by the molecular diffusivity of heat, κ. However, Pe thus defined had very large values around 15000. An alternative definition based upon the length scale Δh (to represent a minimal horizontal length scale of the turbulence within the mean capping inversion) and the turbulent velocity scale of the turbulent elements there (which would still be w_*, approximately) had values of about 4500. This value may perhaps be compared to the value 200 which was considered by Linden & Crapper (1974) to be in the 'low Pe' category. We conclude that Pe probably did not affect Δh, but that it must have helped determine the thickness of the local interface, which is believed to have been on the order of 1 mm in the laboratory.

For the data points in figure 11 representing strong stratification aloft (circles), Δh and $\Delta\theta$ often remained nearly constant during a given experiment as h_0, $\bar{h}$ and Ri^* slowly increased with time. Also, there was very little evidence of a capping inversion (in the mean) in these cases, with $\Delta\theta/\Delta h$ often being somewhat less than $\Gamma = (\partial\bar{\theta}/\partial z)_2$. These are characteristics of 'encroachment', which is a hypothetical non-turbulent entrainment associated with warming or 'filling in' of the mixed layer while $\Delta\theta$ and Δh are considered to be zero (Carson & Smith 1976). From our measurements, however,

we know that the entrainment was highly turbulent and that Δh and $\Delta\theta$ were very substantial in magnitude. The encroachment was thus a 'pseudo-encroachment' (Deardorff 1979) governed by $\Delta\theta$ and Δh remaining nearly constant in time:

$$d\Delta\theta/dt = (dh_2/dt - \overline{w}_2)\,\Gamma - \overline{(w'\theta')}_s/h_0 = 0, \tag{10}$$

where $\overline{w}_2$ is the mean vertical velocity, if any, at $z = h_2$. If $\overline{w}(z) = 0$, equation (10) yields

$$w_e = \overline{(w'\theta')}_s/(h_0\Gamma) \tag{11}$$

for Δh a constant, since then

$$dh_2/dt = d\bar{h}/dt = dh_0/dt = w_e;$$

equation (11) is the well-known encroachment formula.

In our experiments for which Γ is nearly constant and not small relative to $\Delta\theta/\Delta h$, we find that pseudo-encroachment occurred and that $\Gamma\Delta h/\Delta\theta$ lay between 0·9 and 1·5. Thus, a capping inversion is not apparent from the mean temperature data in those experiments, which include all those in table 1 except $E2$, $E5$, $E11$, $E16$, the last part of $E6$ and the first part of $E13$.

As Ri^* increases in figure 11, there is some suggestion that the scatter in $\Delta h/h_0$ increases. That result is also present in the data of Wyatt (1978) from analyses of the shear-driven entrainment experiments of Kantha, Phillips & Azad (1977). For $Ri_* = 35$ she found $\delta h \propto h_0$ with little scatter, where δh is the standard deviation of the local interface $h(x, y, t)$ about its mean position. (From figure 10 we estimate that $\delta h \approx 0{\cdot}2\Delta h$.) For Ri_* as large as 140 there was a factor of 2 scatter in $\delta h/h_0$, and no apparent dependence of δh upon h_0. The comparison between the two different types of experiment is not quantitative, however, because Ri_* is an overall Richardson number based upon the friction velocity, u_*, whereas Ri^* in (7) is based upon the convective velocity scale, w_*.

7. Rate of entrainment

The rate of entrainment, w_e, has been subject to much study because it determines the depth of a turbulent boundary layer at any given time after some initial time at which its depth is known. Considerable success has been attained in relating w_e/u' to a function of $\bar{h}\Delta b/u'^2$ for boundary layers with large Péclet numbers driven by mechanical mixing (Turner 1973) or by shear stress (Kato & Phillips 1969; Kantha *et al.* 1977). The velocity scale u' in the former case is proportional to $K/\bar{h}$, where K is a grid-action parameter with dimensions length squared per time; (see Dickinson & Long 1978) which depends in detail upon the manner in which the turbulence is generated. In the latter case u' is usually considered to be the friction velocity, u_*, although Moore & Long (1971) and Price, Mooers & Van Leer (1978) have instead equated u' to the velocity jump, Δu, across the entrainment zone.

Dependence of entrainment on Ri^*. In turbulence dominated by buoyancy forces, wherein $\bar{h}$ greatly or substantially exceeds the negative Monin–Obukhov length, the appropriate scaling velocity is w_*. The result of plotting $(d\bar{h}/dt - \overline{w}_h)/w_*$ *versus* Ri^* using the data of table 1 is presented in figure 12. The range of Ri^* encompassed here includes most of the (w_* based) values to be expected for atmospheric and oceanic

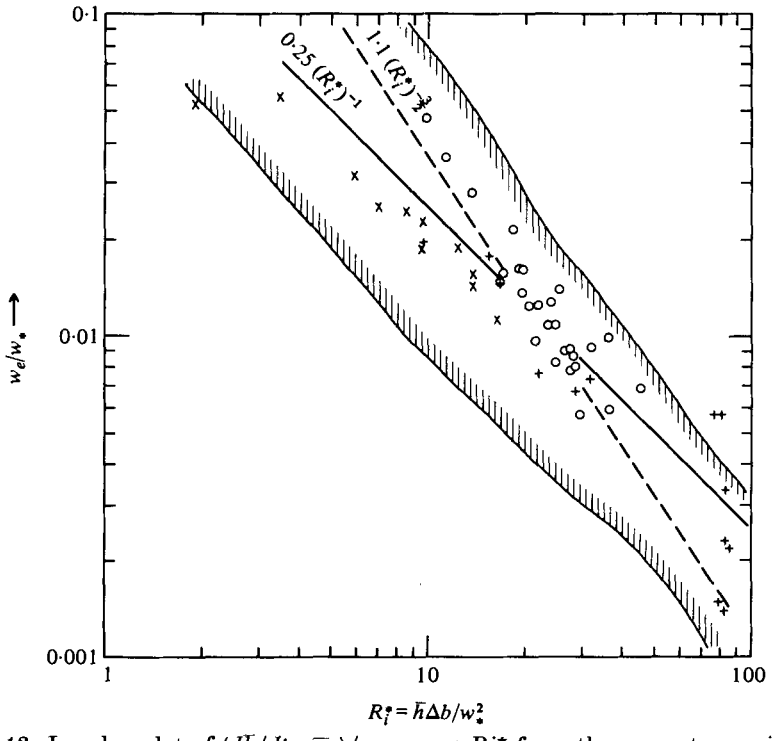

FIGURE 12. Log–log plot of $(d\bar{h}/dt - \overline{w}_h)/w_*$ *versus* Ri^* from the present experiments: ○, data points for which Γ exceeded 5 °C m^{-1} and $\partial\bar{\theta}/\partial z$ was nearly constant above the mixed layer; ×, data for which Γ was less than 5 °C m^{-1} and the fluid configuration was nearly a two-layer system; +, data for which $\partial\bar{\theta}/\partial z$ became less than about 5 °C m^{-1} above a height of $1{\cdot}15h_2$. Hatched envelope contains data spread from experiments of Kantha (1979*c*).

mixed layers. The edged envelope includes the spread of data points from a recent investigation by Kantha (1979) in which the buoyancy force was generated by salinity differences rather than by thermal differences. Although the scatter is great in both sets of experiments, the overall agreement between the two independent approaches supports the belief that a smooth curve faired through the middle of both data sets would represent the most correct estimate. Unfortunately, the data spread does not permit estimating with any certainty whether the $(Ri^*)^{-\frac{3}{2}}$ law (Turner 1973) or the $(Ri^*)^{-1}$ law (Turner 1968) is more appropriate. The latter law, as given by

$$w_e/w_* = 0{\cdot}25(Ri^*)^{-1} \tag{12}$$

is indicated in figure 12. It appears to represent our data slightly better than the $(Ri^*)^{-\frac{3}{2}}$ law. Equation (12) actually follows from the definition of w_* and the commonly used assumptions that

$$w_e = -(\overline{w'b'})_h/\Delta b,$$

$$(\overline{w'b'})_h = -0{\cdot}25(\overline{w'b'})_s,$$

where $(\overline{w'b'})_s$ is the input buoyancy flux at the surface.

As with the $\Delta h/h_0$ data, the w_e/w_* data were found to be essentially reproducible between nearly identical experiments but quite scattered otherwise. In particular, in

the early stages of those experiments which attempted to achieve a two-layer system, w_e/w_* as well as $\Delta h/h_0$ was abnormally large. An example is $E13(a)$ of table 1. It appears that the more rapid entrainment occurring earlier as the heated fluid first fills the lower, nearly neutral layer persists for some time afterwards while Ri^* rapidly increases. Thus, a unique dependence upon Ri^* may not be achieved if

$$(\bar{h}/w_*)\,|dRi^*/dt|$$

exceeds a number of order unity. None of the scatter at large Ri^* can be attributed to Pe effects since, in these experiments, Pe was relatively constant. At small Ri^* of order 1 or 2 and less a flattening of w_e/w_* is expected as a maximum limiting value is approached. This limiting value will be discussed at the end of this section.

It might be thought that an entrainment theory which recognizes the finite value of Δh and allows for it to change with time would perform better than (12). An entrainment relation of Deardorff (1979, equation (30)) is of this type, and utilizes the same definition of Δh as used herein. When tested, results from that relationship were not quite as good, however, as the use of (12) (for which the root-mean-square deviation in observed values of Ri^*w_e/w_* from 0·25 turned out to be 0·084). Apparently, in Deardorff's (1979) treatment the calculated entrainment is quite sensitive to the assumption that $\partial\bar{\theta}/\partial z = 0$ at $z = h_0$ and below. Values of $(d\Delta h/dt - \Delta w)$ are included in table 1, where $\Delta w = \bar{w}_2 - \bar{w}_0$, to permit theories which involve Δh to be tested.

Relation between (11) *and* (12). The relation between pseudo-encroachment from (11) and entrainment predicted from (12) is quite direct. If in Ri^* the quantity $\Delta\theta$ is replaced by $\Gamma\Delta h/G$, where

$$G \equiv \Gamma\Delta h/\Delta\theta,$$

(12) becomes

$$w_e = 0{\cdot}25G\overline{(w'\theta')}_s/\Gamma(\Delta h). \tag{13}$$

Since for pseudo-encroachment $G \approx 1$, and since $\Delta h = 0{\cdot}25h_0$ is often a good approximation, (13) then becomes synonymous with (11). (The tendency for G to exceed unity by some 20 % is often balanced by Δh tending to exceed $0{\cdot}25h_0$ by a similar amount.) Thus, (12) is as valid for cases of pseudo-encroachment as it is for the two-layer system even though (12) does not explicitly contain Γ.

Entrainment versus stratification of outer layer. Kantha *et al.* (1977) and Linden (1975) have concluded that for a given value of overall Richardson number the dimensionless entrainment rate is very noticeably greater for a two-layer system than for the stably stratified outer layer. Their possible explanation at that time invoked the export of energy from the mixed layer to internal gravity waves in the stable outer layer in the latter case. This removes kinetic energy that might otherwise be utilized for entrainment. In comparing the circles and crosses in figure 12, we find no evidence that this result holds for convectively driven turbulence. More recently, Kantha (1979*a*) has argued that the energy drain by internal waves is too small to affect the entrainment rate in most cases of interest, and our results support this latter conclusion. Entrainment-rate discrepancies between the shear-stress experiments of Kato & Phillips (1969) which utilized a stable outer layer and those of Kantha *et al.* (1977) which were of the two-layer type are now believed to be associated with the importance of the velocity jump across Δh in addition to the friction velocity (Price 1979; Kantha 1979*b*).

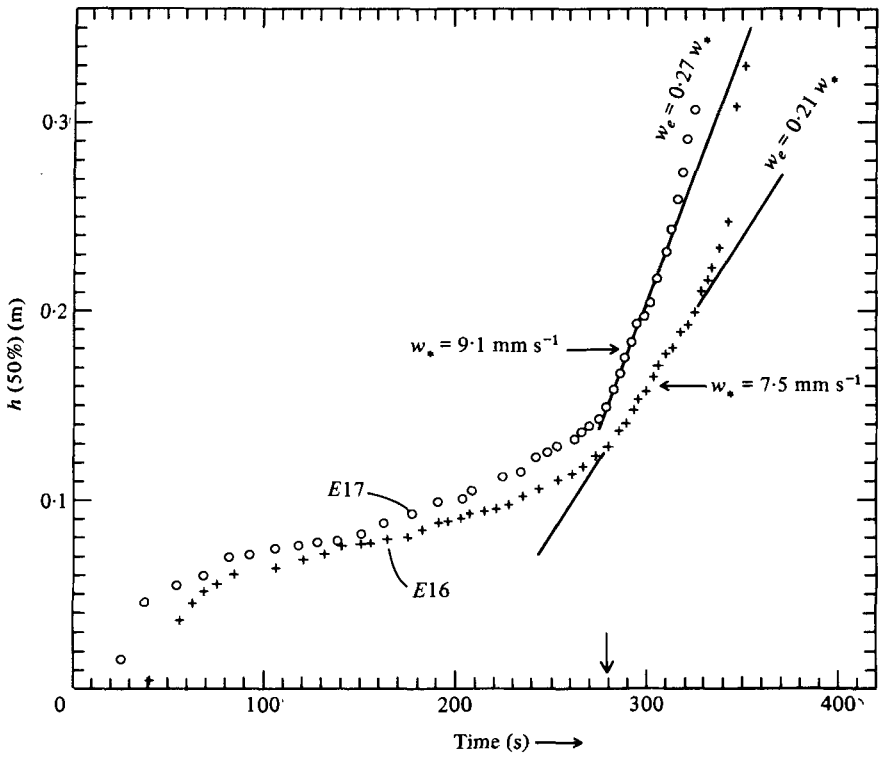

FIGURE 13. Time variation of the height of 50 % mixed-layer cover, $h(50\,\%)$, for experiments $E16$ and $E17$ (the latter not tabulated). Arrow on abscissa denotes time at which $\Delta\theta$ reached zero and free entrainment commenced into a neutral layer aloft.

Entrainment into a neutral layer. In the latter stage of $E16$ and in an additional experiment ($E17$), $d\bar{h}/dt$ was measured in the absence of subsidence during and shortly after the time that Δb, i.e. $\Delta\theta$, had become zero and entrainment was proceeding at a maximum rate into a neutral layer. In these two cases $\bar{h}$ will refer to the height of 50 % mixed-layer cover as determined with the aid of the horizontally spread laser beam. (Estimates of dh_2/dt during the same time periods proved too highly variable to be statistically significant, although dh_2/dt did then substantially exceed $d\bar{h}/dt$.) The two experiments were very similar except that in $E16$ the surface heat flux was some 40 % smaller.

The growth of $\bar{h}$ in these two experiments is shown in figure 13. The arrow on the abscissa denotes the time, which happened to be the same in each case, at which $\Delta\theta$ was estimated to have first reached zero, judging from the temperature records. In each case a section of enhanced growth rate commences at this time. The respective growth rates are $0{\cdot}21w_*$ and $0{\cdot}27w_*$. Assuming this difference in values reflects sampling error, we find that on the average for free entrainment

$$(d\bar{h}/dt - \overline{w}_h)/w_* = 0{\cdot}24(1 \pm 0{\cdot}12). \tag{14}$$

This value agrees well with a previous estimate derived from numerical modelling of the atmospheric boundary layer by Deardorff (1974).

Usually, this stage of entrainment is very brief because a new stable layer is quickly

encountered by h_2. Another reason, which was even more relevant in our experiments, is that the fluid becomes somewhat unstably stratified, on the horizontal average, out to $z = \bar{h}$ if the entrainment into the neutral layer persists for a little while. Thus, $d\bar{h}/dt$ in figure 13 (uppermost data points) soon exceeded substantially the limiting rate given by (14) for mixed-layer advancement into a neutral layer.

8. Discussion

Some of the mixed-layer growth theories which have permitted the capping inversion to have a finite thickness have attempted to predict Δh or related thickness by means of parcel overshoot theory in which the restoring buoyancy force is made proportional to $g\beta\Gamma\Delta h$ (e.g., see Zeman & Tennekes 1977). From § 3, however, it is instead seen that the maximum restoring buoyancy force is proportional to $g\beta\Delta\theta$, since by its very definition $\Delta\theta$ represents the maximum negative temperature anomaly a penetrating parcel experiences. Except for cases of pseudo-encroachment, the quantities $\Delta\theta$ and $\Gamma\Delta h$ are not related to each other. Although the parameter Γ is of primary importance in determining how $\Delta\theta$ evolves with time, it would seem to be of little or no importance in determining Δh at any given time.

A simplistic picture commonly held of the mixed-layer top is that of a continuous interface, possibly multivalued at some places, which locally undergoes contortions and undulations but remains intact. It has probably been known for some time that this picture is not very accurate because of entrainment, and in § 4 it was seen that some of the entrainment cusps or wedges have diameters much in excess of the Kolmogorov length scale at heights below h_0. Thus along such paths of entraining fluid the local interface is absent. The simple picture becomes even more inaccurate when significant amounts of detrained fluid are recognized to exist. It seems to require a subjective decision to estimate at what point a tongue of detraining fluid can no longer be considered mixed-layer fluid, or at what value a threshold should be set that would locally discriminate between turbulent and non-turbulent fluid.

The definitions of h_2 and h_0, along with the thickness of the entrainment zone, are also open to debate. Although we have defined h_2 as the maximum height reached anywhere in our laboratory tank by a parcel of mixed-layer fluid at any given time (as smoothed subsequently in time), the equivalent definition for geophysical use would be the height at which $A(z)$ has decreased to a small value such as 0·01. We prefer a very small mixed-layer fraction for the h_2 criterion because equation (10) incorporates the assumption that $\partial(\overline{w'\theta'})/\partial z = 0$ at and above $z = h_2$, a result which approximately holds only after a height is reached beyond which scarcely any mixed-layer fluid has penetrated. Knowledge of h_2 is mandatory for developing and testing mixed-layer growth theories which involve estimates of $\Delta\theta$ and which, therefore, require use of (10); only when h_2 is known can Γ and $\Delta\theta$ be estimated from observations.

We have found no evidence that significant amounts of heat flux near or above $z = h_2$ are carried by growing internal waves (Deardorff 1969), a possibility that would greatly complicate the determination of h_2. However we cannot rule out experimentally this possibility for turbulent heat fluxes smaller in magnitude than about 0·1 of the most negative turbulent heat flux existing at $z = \bar{h}$, owing to the weak secondary circulations existing in the laboratory tank.

For h_0, a definition that $A(z)$ lie in the vicinity of 0·9 or 0·95 would seem to be

appropriate and more general than that used herein (that it be the height where the buoyancy flux first crosses zero). Not only would such an $A(h_0)$ definition coincide approximately with the latter one for convectively mixed layers, but it would permit the same definition to be used for mixed layers stirred by mechanical turbulence or shear-generated turbulence in addition to, or in place of, buoyancy-generated turbulence.

It should be noted that little or no information about Δh can be deduced from an individual density or temperature sounding. Any particular sounding may chance to pass through an active mixed-layer dome or hummock, for which a single jump in density or temperature would occur over an extremely small height interval. Or it may pass through a region where entrained fluid is partially engulfed at several different heights, leading to several smaller jumps in temperature or density; or along a continuing path of entrainment where no distinct jump in properties may be evident. Only the average of several (or many) soundings, preferably nearly simultaneous and separated in space by distances on the order of $\bar{h}$, can give reliable estimates of the thickness of the entrainment zone and properties at its lower and upper edges. However, in the atmosphere the use of only a few soundings, when coupled with the use of an S-band radar (e.g., see Hardy & Ottersten 1969), a lidar (e.g., see Kunkel, Eloranta & Shipley 1977), and/or the acoustic sounder (see Hall, Edinger & Neff 1975), can alleviate these problems. Direct estimates of h_2 from such equipment are especially valuable for its determination when the lapse rate in the unmodified fluid aloft is variable and h_2 otherwise uncertain.

9. Conclusions

(i) For a convectively mixed layer driven by buoyancy input at the surface, the entrainment zone is conveniently defined as the layer (Δh) where the mean buoyancy flux is negative (due to entrainment).

(ii) With this definition, the upper edge of the entrainment zone is found to coincide with the greatest height reached by but a very a small fraction of overshooting mixed-layer elements. The lower edge is usually found to lie at a height where mixed-layer fluid occupies 90 % to 95 % of the area.

(iii) The mean height of the mixed layer, previously defined as the height of most negative mean buoyancy flux, is found to agree roughly with the height at which mixed-layer fluid occupies one-half the area.

(iv) For values of overall Richardson number (Ri^* of (7)) commonly found in the atmospheric mixed layer, the entrainment zone as determined in the laboratory has a thickness of some 20 % to 40 % of the well-mixed depth (h_0). (Horizontal inhomogeneities over land, especially of surface temperature, may increase $\Delta h/h_0$ substantially beyond these values.) The tentative dependence of $\Delta h/h_0$ upon Ri^* is found to be

$$\Delta h/h_0 = 0{\cdot}21 + 1{\cdot}31(Ri^*)^{-1}$$

above an ideal, horizontally homogeneous surface.

(v) When the mixed layer grows into a region where $\partial\theta/\partial z$ is constant and of significant magnitude, both Δh and $\Delta\theta$ tend to be constant in time and pseudo-encroachment (see (11)) occurs. An indicator of its occurrence appears to be that Γ

equal or exceed $\Delta\theta/\Delta h$, which means that no distinct capping inversion is then noticeable in a horizontal-mean temperature sounding.

(vi) When the mixed layer grows into a neutral layer, the rate of advancement of the 50 % coverage height is found to be

$$w_e = 0{\cdot}24(1 \pm 0{\cdot}12)\, w_*.$$

(vii) An entrainment rate relation which adequately fits the present data is

$$w_e/w_* = 0{\cdot}25(Ri^*)^{-1}$$

although a dependence as steep as $(Ri^*)^{-\frac{3}{2}}$ cannot be ruled out because of data scatter.

(viii) Temporary detrainment of mixed-layer fluid is an important process within the entrainment zone. At any given time, up to 30 % of the mixed-layer matter near the middle of the entrainment zone appears to be partially diluted detrained debris.

(ix) Because of both detrainment and entrainment, the outer edge of the mixed layer cannot be rigorously treated as a continuous, intact undulating surface. Its precise local placement moreover depends upon whether its definition is based upon a contrast in intensity of vorticity or turbulence, or upon contrast in concentration of a conservative Lagrangian tracer.

(x) The uppermost hummocks or domes of the convectively mixed layer in our laboratory closely resemble cumulus-humilis clouds.

The work performed in this study was supported by the Meteorology Program, Division of Atmospheric Sciences, of the National Science Foundation under Grant no. ATM77-24507. We are indebted to Mr Mike Drost for preparing software with which to read digital tapes on the Oregon State University CYBER computer, and to Professor Larry Gates and Dean Krauss for making the laboratory facility a reality within the Department of Atmospheric Sciences.

Appendix

To obtain (6), the simplified vertical equation of motion following a parcel is utilized:

$$w\,dw/dz = -g\beta(\theta - \theta_{en}), \tag{A 1}$$

where θ is the parcel temperature identified with the mixed-layer mean value, θ_m, and θ_{en} is identified as environmental fluid existing just outside the mixed layer, as in a two-layer system. Integration from $z = h_0$, where $w = w_0$, to $z = h_2$, where w of the effective parcel is just zero, produces

$$w_0^2 = 2g\beta\Delta\theta\Delta h. \tag{A 2}$$

Upon assuming

$$w_0^2/w_*^2 = c'' \tag{A 3}$$

we obtain, approximately,

$$\Delta h/h_0 = \tfrac{1}{2}c''(Ri^*)^{-1} \tag{A 4}$$

as in (6).

We may note, however, that in place of θ_{en} in (A 1) we should use the horizontally averaged value, $\bar{\theta}$, as defined in (4*a*). Then the vertical velocity of the parcel will be

reckoned relative to zero, as desired, when $\overline{w} = 0$, and a parcel may be considered as rising within a pre-existing mixed-layer dome. Thus (A 1) becomes

$$w\,dw/d\zeta = -[1-A(\zeta)]g\beta\Delta\theta\Delta h, \tag{A 5}$$

where dz has been replaced by $\zeta\Delta h$ (see (1)). Upon parametrizing $A(\zeta)$ in figures 5 and 6 by the cubic polynomial

$$A(\zeta) = 0{\cdot}95 - 0{\cdot}26\zeta - 2{\cdot}33\zeta^2 + 1{\cdot}64\zeta^3 \tag{A 6}$$

we find that vertical integration from $\zeta = 0$ to $\zeta = 1$ yields

$$\Delta h/h_0 = 0{\cdot}9c''(Ri^*)^{-1}, \tag{A 7}$$

which differs from (A 4) only in the greater magnitude of the proportionality constant.

In order to obtain behaviour of $\Delta h/h_0$ which approximates that observed, while retaining the present simplification of the parcel framework, we must postulate that w_0/w_* in (A 3) is a function of Ri^*. Only upon assuming

$$w_0^2/w_*^2 = 1{\cdot}46 + 0{\cdot}23Ri^* \tag{A 8}$$

do we obtain

$$\Delta h/h_0 = 0{\cdot}21 + 1{\cdot}31(Ri^*)^{-1} \tag{A 9}$$

as in (9).

Any attempt to rationalize (A 8) will recognize that w_0 typifies a vertical velocity at h_0 far out along the positive tail of the w frequency distribution. For $Ri^* = 10$, for example, and for $\sigma_w^2(h_0)/w_*^2 = 0{\cdot}2$ from Willis & Deardorff (1974), one finds that $w_0 = 4{\cdot}3\sigma_w$, where σ_w is the standard deviation in w. Such a value, though large, may not be too unreasonable. However, (A 8) is unreasonable for large Ri^*. The inference is that the simplistic parcel theory suffers grave errors that become intolerable with increasing Ri^*.

REFERENCES

Betts, A. K. 1973 Non-precipitating cumulus convection and its parameterization. *Quart. J. Roy. Met. Soc.* **99**, 178–196.

Betts, A. K. 1976 Modeling subcloud layer structure and interaction with a shallow cumulus layer. *J. Atmos. Sci.* **33**, 2363–2382.

Carson, D. J. & Smith, F. B. 1974 Thermodynamic model for the development of a convectively unstable boundary layer. In *Advances in Geophysics*, vol. 18A (ed. H. E. Landsberg & J. Van Mieghem), pp. 111–124. Academic.

Deardorff, J. W. 1969 Numerical study of heat transport by internal gravity waves above a growing unstable layer. *Phys. Fluids Suppl.* II 184–194.

Deardorff, J. W. 1974 Three-dimensional numerical study of the height and mean structure of a heated planetary boundary layer. *Boundary-Layer Met.* **7**, 81–106.

Deardorff, J. W. 1976 On the entrainment of a stratocumulus-topped mixed layer. *Quart. J. Roy. Met. Soc.* **102**, 563–582.

Deardorff, J. W. 1979 Prediction of convective mixed-layer entrainment for realistic capping inversion structure. *J. Atmos. Sci.* **36**, 424–436.

Deardorff, J. W., Willis, G. E. & Lilly, D. K. 1969 Laboratory investigation of non-steady penetrative convection. *J. Fluid Mech.* **35**, 7–31.

Dickinson, S. C. & Long, R. R. 1978 Laboratory study of the growth of a turbulent layer of fluid. *Phys. Fluids* **21**, 1698–1701.

Gaynor, J. E. & Mandics, P. A. 1978 Analysis of the tropical marine boundary layer during GATE using acoustic sounder data. *Mon. Weath. Rev.* **106**, 223–232.

GOODMAN, J. K. & MILLER, A. 1976 Mass transport across a temperature inversion. *San Jose State Univ., Dept. of Met., Rep.* no. 76-10.

HALL, F. F., EDINGER, J. G. & NEFF, W. D. 1975 Convective plumes in the planetary boundary layer, investigated with an acoustic sounder. *J. Appl. Met.* **14**, 513–523.

HARDY, K. R. & OTTERSTEN, H. 1969 Radar investigations of convective patterns in the clear atmosphere. *J. Atmos. Sci.* **26**, 666–672.

KAHN, P. H. & BUSINGER, J. A. 1978 The effect of radiative flux divergence on entrainment of a saturated convective boundary layer. *Quart. J. Roy. Met. Soc.* **105**, 303–305.

KANTHA, L. H. 1979*a* On generation of internal waves by turbulence in the mixed layer. *Dyn. Atmos. & Oceans* **3**, 39–46.

KANTHA, L. H. 1979*b* Comparison of Kantha entrainment model with other slab models. *Ocean Modelling* **26**, 6–9. D.A.M.T.P., University of Cambridge.

KANTHA, L. H. 1979*c* Turbulent entrainment at a bouyancy interface due to convective turbulence. Unpublished manuscript, Dept. of Earth and Plan. Sci., Johns Hopkins Univ., Baltimore, Maryland 21218.

KANTHA, L. H., PHILLIPS, O. M. & AZAD, R. S. 1977 On turbulent entrainment at a stable density interface. *J. Fluid Mech.* **79**, 753–768.

KATO, H. & PHILLIPS, O. M. 1969 On the penetration of a turbulent layer into stratified fluid. *J. Fluid Mech.* **37**, 643–655.

KUNKEL, K. E., ELORANTA, E. W. & SHIPLEY, S. T. 1977 Lidar observations of the convective boundary layer. *J. Appl. Met.* **16**, 1306–1311.

LILLY, D. K. & SCHUBERT, W. H. 1979 The effects of radiative cooling in a cloud-topped mixed layer. *J. Atmos. Sci.* **37**, 482–487.

LINDEN, P. F. 1975 The deepening of a mixed layer in a stratified fluid. *J. Fluid Mech.* **71**, 385–405.

LINDEN, P. F. & CRAPPER, P. F. 1974 Effect of molecular diffusion on the structure of a turbulent density interface. In *Advances in Geophysics*, vol. 18A (ed. H. E. Landsberg & J. Van Mieghem), pp. 433–443. Academic.

LONG, R. R. & KANTHA, L. H. 1978 The rise of a strong inversion caused by heating at the ground. In *Proc. 12th Naval Hydrodyn. Symp., Wash. D.C.* National Academy of Sciences.

MALKUS, J. S. 1958 On the structure of the trade wind moist layer. *Papers in Phys. Oceanog. & Met.* **13**, M.I.T. and Woods Hole Oceanog. Inst. 1–48.

MOORE, M. J. & LONG, R. R. 1971 An experimental investigation of turbulent stratified shearing flow. *J. Fluid Mech.* **49**, 635–655.

NAMIAS, J. 1939 On the dissipation of tall cumulus clouds. *Monthly Weather Rev.* **67**, 294-295.

PHILLIPS, O. M. 1972 The entrainment interface. *J. Fluid Mech.* **51**, 97–118.

PHILLIPS, O. M. 1977 *The Dynamics of the Upper Ocean.* 2nd edn. Cambridge University Press.

PRICE, J. F. 1979 Observations of a rain-formed mixed layer. *J. Phys. Oceanog.* **9**, 643–649.

PRICE, J. F., MOOERS, C. N. K. & VAN LEER, J. C. 1978 Observation and simulation of storm-induced mixed-layer deepening. *J. Phys. Oceanog.* **8**, 582–599.

RANDALL, D. A. 1980 Entrainment into a stratocumulus layer with distributed radiative cooling. *J. Atmos. Sci.* **37**, 148–159.

RAYMENT, R. & READINGS, C. J. 1974 A case study of the structure and energetics of an inversion. *Quart. J. Roy. Met. Soc.* **100**, 221-233.

TURNER, J. S. 1968 The influence of molecular diffusivity on turbulent entrainment across a density interface. *J. Fluid Mech.* **23**, 639–656.

TURNER, J. S. 1973 *Buoyancy Effects in Fluids.* Cambridge University Press.

UTHE, E. E. 1972 Lidar observations of the urban aerosol structure. *Bull. Am. Met. Soc.* **53**, 358–360.

WILLIS, G. E. & DEARDORFF, J. W. 1974 A laboratory model of the unstable planetary boundary layer. *J. Atmos. Sci.* **31**, 1297–1307.

WYATT, L. R. 1978 The entrainment interface in a stratified fluid. *J. Fluid Mech.* **86**, 293-311.

ZEMAN, O. & TENNEKES, H. 1977 Parameterization of the turbulent energy budget at the top of the daytime atmospheric boundary layer. *J. Atmos. Sci.* **34**, 111–123.

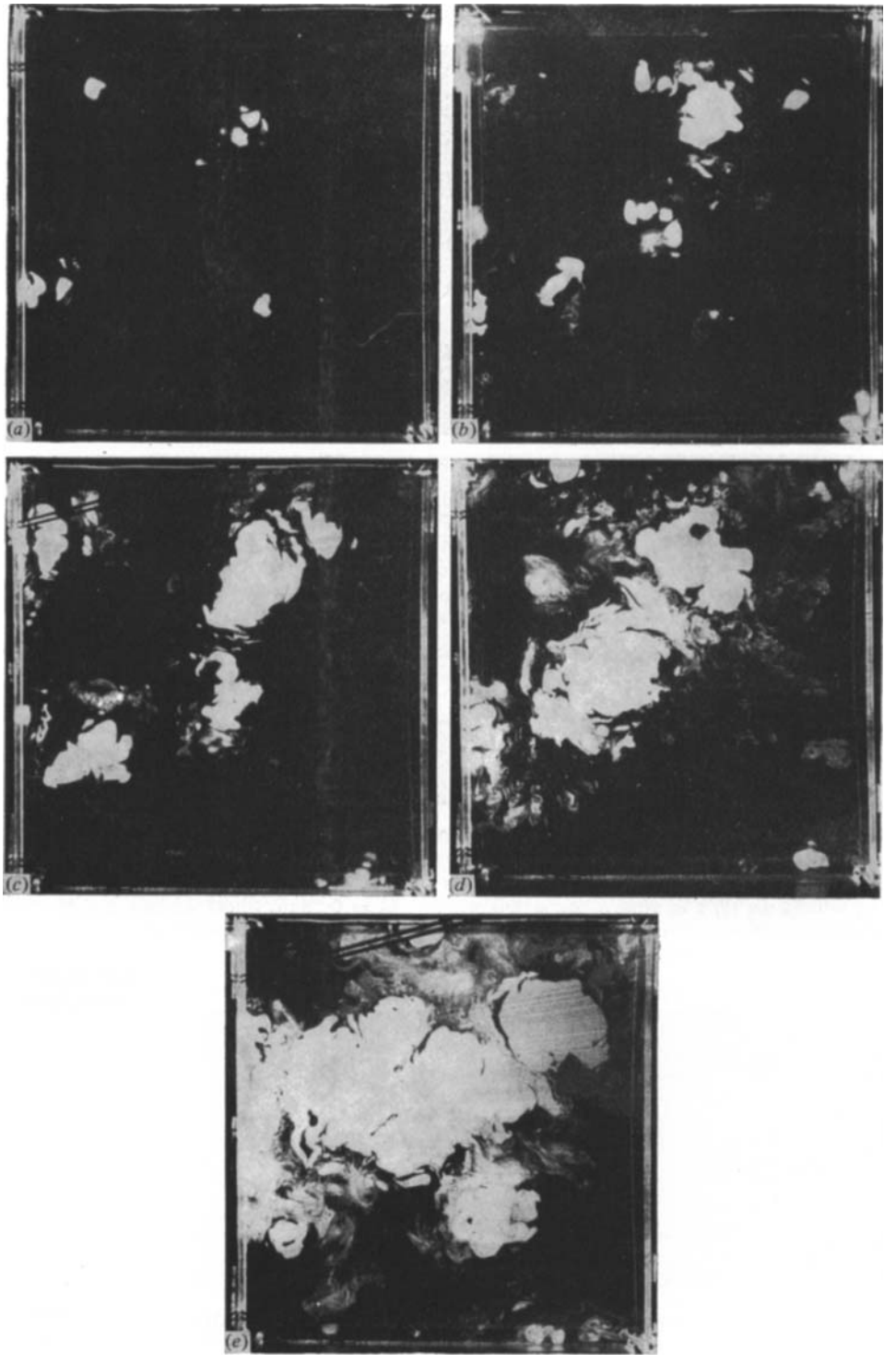

FIGURE 2. Plan-view photographs from experiment $E7$ of mixed-layer fluid rendered visible by a dilute milk solution intercepted by the horizontally spread laser beam at a height of 0·278 m. Light beam passes from left to right. (*a*) $t = 513$ s, $\zeta = 0{\cdot}87$; (*b*) $t = 611$ s, $\zeta = 0{\cdot}77$; (*c*) $t = 673$ s, $\zeta = 0{\cdot}71$; (*d*) $t = 719$ s, $\zeta = 0{\cdot}60$; (*e*) $t = 1040$ s, $\zeta = 0{\cdot}46$; $t = 0$ corresponds to the approximate time of initiation of the convection.

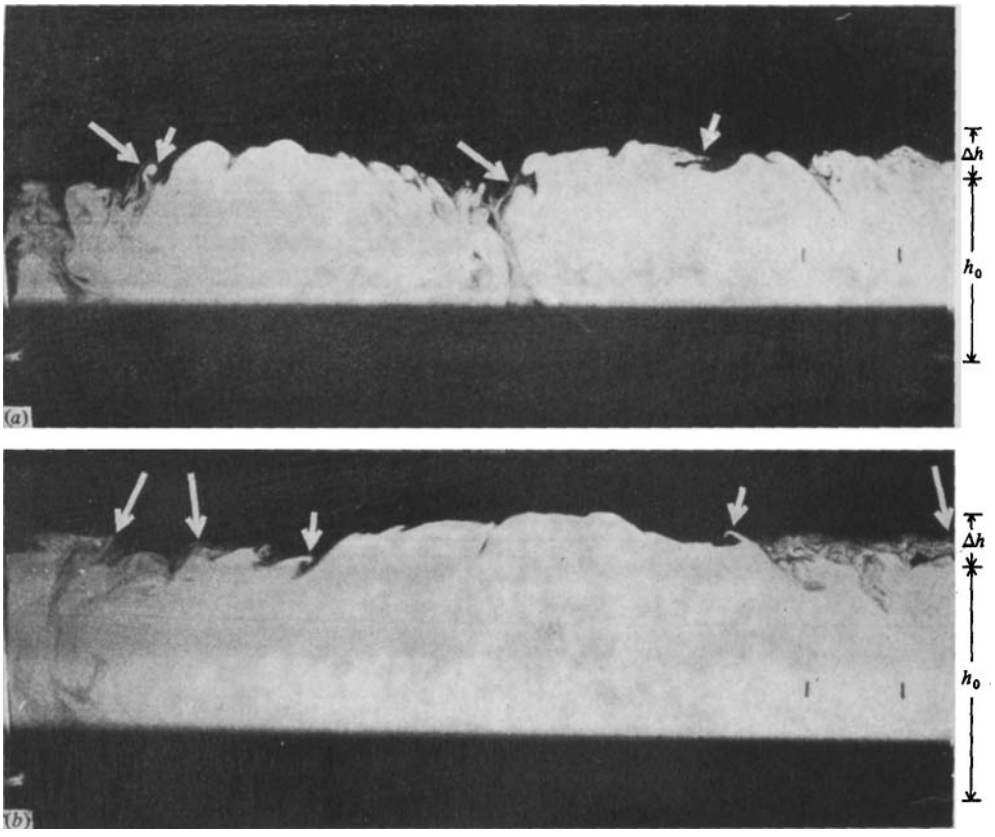

FIGURE 9. Side views of a vertical slice of the mixed layer along the centre of the convection tank .Distance between tick marks at right side in each photo is 0·113 m. Light passes from right to left. The average Kolmogorov length is 1·2 mm within Δh. (*a*) $t = 363$ s, $w_* = 9{\cdot}3$ mm s^{-1}, $h_0 = 0{\cdot}23$ m; (*b*) $t = 1068$ s, $w_* = 8{\cdot}8$ mm s^{-1}, $h_0 = 0{\cdot}28$ m. Short arrows denote some of the regions in which active detrainment is under way; long arrows point to matter that can be considered already detrained.

FIGURE 10. Oblique view from above of uppermost hummocks of the mixed layer at time $t = 320$ s in an experiment like *E*6, showing the resemblance to cumulus-humilis clouds. Illumination is from both sides and is blocked below the simulated cumulus cloud base at a height of about 0·28 m. Converging lines on the left and right side walls are located at a height of 0·31 m, and are a distance 1·14 m apart.